# JOINT X-RAY AND NEUTRON TOMOGRAPHY OF SHALE CORES FOR CHARACTERIZING STRUCTURAL MORPHOLOGY

Wei-Shan Chiang [1, 2, 3], Jacob M. LaManna [4], Alexander Katsevich [5, 6], Daniel S. Hussey [4], David L. Jacobson [4], Michael Frenkel [5], Daniel T. Georgi [1], Qiushi Sun [1], Yun Liu [2, 3, 7], and Jin-Hong Chen [1]

[1] Reservoir Engineering Technology, Aramco Research Center – Houston, TX 77084
[2] Center for Neutron Research, NIST, Gaithersburg, MD 20899
[3] Department of Chemical & Biomolecular Engineering, U. Delaware, DE 19716
[4] Physical Measurement Laboratory, NIST, Gaithersburg, MD 20899
[5] iTomography Corporation, Houston, TX 77021
[6] University of Central Florida, Orlando, FL 32816
[7] Department of Physics and Astronomy, University of Delaware, Newark, DE 19716

*This paper was prepared for presentation at the International Symposium of the Society of Core Analysts held in Vienna, Austria, 27 August – 1 September 2017*

## ABSTRACT

To better model the storage and flow of gas and light hydrocarbons in shales, it is necessary to quantify the structural distributions of organic and inorganic components and fractures in shales over a large range of length scales. The combination of neutron and X-ray tomography provides these distributions on the core scale, in contrast to most current μm-scale SEM studies.

We present a new conjoint X-ray and neutron computed tomography (CT) for 3D shale-core characterization. Neutrons are attenuated significantly by hydrogen compared with most other elements. Therefore, the hydrogen-rich areas, i.e. organic matter can be easily distinguished from fractures and inorganic, hydrogen-poor matter. On the other hand, X-rays are attenuated more when the atomic number *Z* of the element is larger and can be used to identify high-*Z* elements such as minerals. Therefore, combining X-ray and neutron tomography can provide much more comprehensive information of shale. The combination of neutron and X-ray tomography allows one to identify different minerals, fractures, and organic matter for improved and more realistic representation of the rock 3D structure.

## INTRODUCTION

Natural gas production worldwide from shale reservoirs has played an important role for the global energy supplies [1]. Despite its success, many fundamental issues in the gas storage and gas transport are not clearly addressed. It has been reported that most natural gases in shale rocks are stored in kerogens that contain

pores with the characteristic length scale between 1 to 100 nm. Traditional 2D Scanning Electron Microscopy (SEM) and 3D Focused Ion Beam-SEM (FIB-SEM) have successfully revealed the structures of shale rocks at very small length scales comparable to the pores. However, it is also critically important to identify the kerogen distribution at the core scale so that a more statistically representative characterisation of the sample can be constructed to understand the gas flow.

Both neutron and X-ray tomography techniques are widely used to probe a wide range of materials. They are very useful to investigate shale rocks at the core scale. The X-ray tomography technique is more sensitive to the heavy elements with large atomic number $Z$ because X-rays interact with the electron cloud of the elements. Thus, X-ray imaging can easily probe minerals in rocks. Unlike X-rays, there is little correlation of neutron cross sections with atomic number. In particular, neutrons are very sensitive to hydrogen rich materials. Water and organic matter in shale rocks, such as kerogen, bitumen, and heavier immobile hydrocarbons can strongly attenuate neutrons. Thus, neutron imaging is very useful to probe the distribution of hydrogen rich materials. Since the sensitivity for X-rays and neutrons to different elements are very distinct, studying the same rock with both X-ray and neutron imaging techniques can provide more useful information that may not be clearly understood by using only one of them [2]. Dual, sequential neutron and X-ray tomography (i.e. different facilities) has been successfully applied to many other materials such as fuel cells [3], [4], batteries [5], and cultural heritage objects [6], [7].

In this study, we illustrate the use of dual X-ray and neutron tomography to study shales at the core scale. The distributions of minerals, organic matter, and fractures are successfully identified in a Middle Eastern shale.

## ATTENUATION OF X-RAY AND NEUTRON

X-ray tomography and neutron tomography are both non-invasive methods and have similar principles. The beam intensity after passing through a sample can be expressed as

$$I_t(l) = I_0\, e^{-\int_l \mu(x)dx} \qquad (1)$$

$l$ denotes the transmission path and $x$ is a 3-dimensional position vector. The attenuation coefficient, $\mu$, is related to the attenuation cross sections through

$$\mu = \sum_i \sigma_{t,i}\, N_i \qquad (2)$$

$\sigma_{t,i}$ is the total attenuation cross section for X-ray or neutron and $N_i$ is the number density of type $i$ atom.

**Table 1**. The attenuation coefficient for X-ray and neutron for typical constituents in shales.

| Component | | $\mu$ for X-ray 99.2 keV[a] ($cm^{-1}$) | $\mu$ for neutron 1.8 Å[b] ($cm^{-1}$) |
|---|---|---|---|
| Kerogen[c] | ($C_{100}H_{161}N_{1.85}S_{0.7}O_{9.2}$) | 0.22 | 6.97 |
| Quartz | ($SiO_2$) | 0.45 | 0.29 |
| Pyrite | ($FeS_2$) | 1.41 | 0.44 |
| Siderite | ($FeCO_3$) | 1.03 | 0.67 |
| Calcite | ($CaCO_3$) | 0.53 | 0.35 |
| Dolomite | ($CaMg(CO_3)_2$) | 0.51 | 0.41 |
| Anhydrite | ($CaSO_4$) | 0.58 | 0.29 |
| Celestine | ($SrSO_4$) | 1.95 | 0.34 |
| Kaolinite | ($Al_2Si_2O_5(OH)_4$) | 0.45 | 2.32 |
| Chlorite | ($Mg_5Al_2Si_3O_{10}(OH)_8$) | 0.42 | 2.07 |
| Daphnite | ($Fe_5Al_2Si_3O_{10}(OH)_8$) | 0.82 | 2.30 |
| $H_2O$ | | 0.17 | 5.65 |
| $C_6H_{14}$ | | 0.11 | 5.39 |

[a] 99.2 keV is the mean incident energy of X-ray to the sample and attenuation coefficient for X-ray is obtained from the X-Ray Form Factor, Attenuation, and Scattering Tables [9]. [b] The neutrons used in this study are thermal neutrons with a distribution of wavelength centered around 1.8 Å. The attenuation coefficient for neutron is obtained from Neutron Activation and Scattering Calculator [8]. [c] Kerogen formula obtained from literature [23] and the density used is 1.3 g/cm$^3$.

Table 1 lists the attenuation coefficient, $\mu$, for several common elements found in shales for X-ray and neutron at relevant conditions. Attenuation coefficients for neutrons and X-rays are calculated by using Neutron Activation and Scattering Calculator provided by National Institute of Standards and Technology (NIST) Center for Neutron Research (NCNR) [8] and X-Ray Form Factor, Attenuation, and Scattering Tables provided by NIST Physical Measurement Laboratory [9], respectively. Clearly, hydrogen containing materials have larger attenuation coefficients for neutrons.

In X-ray imaging, $\mu$ of organic matter is small compared with the minerals but close to the empty space, i.e. the fractures. It is hard to distinguish between kerogen and fracture using only X-ray data. In contrast, kerogen and any components with a large amount of hydrogens have large $\mu$ for neutrons compared to hydrogen-poor minerals: in neutron imaging, $\mu$ is 6.97 $cm^{-1}$ for kerogen while $\mu$ is only 2.07 $cm^{-1}$ to 2.32 $cm^{-1}$ for clay minerals and below 0.7 $cm^{-1}$ for most of the other shale forming minerals. Thus, kerogen can be easily distinguished from minerals and open fractures using neutron data. In X-ray imaging $\mu$ for kerogen is about

half of $\mu$ for quartz and some major clays. Overall, the neutron attenuation coefficient provides higher contrast for organic matter than does the X-ray attenuation coefficient.

## CORE PLUG SAMPLE

An organic-rich and carbonate-rich source rock sample from Middle East shale was used for this study. The sample was 25 mm in diameter and approximately 19 mm in length. The surfaces on the two ends of the sample are in their original state without being trimmed. Thus, they have rough surface and are not flat.

## NEUTRON TOMOGRAPHY

Neutron tomography was conducted at the NCNR at the BT2 neutron imaging facility. This instrument offers a high thermal neutron flux for radiography. Full details of the instrument and applied neutron data reconstruction technique can be found in the following manuscript [10]. Detector resolution was set to 30 µm to keep the sample in the field-of-view at all projection angles. The scan took approximately 18 hours to complete. Volumes were reconstructed from the projection images using the commercial CT software package Octopus[1] using the parallel beam filtered back projection algorithm and visualized with the open-source Drishti Volume Exploration Tool [11].

## HELICAL X-RAY TOMOGRAPHY

The raw X-ray projection data was collected at the Aramco Research Center in Houston using a North Star Imaging X5000 Industrial CT Scanner (NSI). The helical cone-beam CT scan was performed using a voltage of 160 keV and a current of 120 µA. The Source-Isocenter Distance (SID) and the Source-Detector Distance (SDD) were 92.2 mm and 999 mm, respectively; 720 projections per revolution were taken over 7 revolutions with a helical pitch of 10 mm per revolution. For the purposes of noise reduction, 8 frames were averaged per radiograph. The magnification factor of 10.8 allows one to achieve a voxel dimension about 20 µm. After the scan, the raw projection CT data was transferred to a stand-alone single GPU laptop to perform raw CT data preprocessing and helical image reconstruction using the iTomography KFBP software package1. Prior to applying 3D image reconstruction, we applied routines to detect and correct bad pixels and accurately determine the central ray position [13], [15].

[1]Certain trade names and company products are mentioned in the text or identified in an illustration in order to adequately specify the experimental procedure and equipment used. In no case does such identification imply recommendation or endorsement by the National Institute of Standards and Technology or Aramco Services Company, nor does it imply that the products are necessarily the best available for the purpose.

*X-ray CT Reconstruction* The volume was reconstructed from the projection images using the theoretically exact Katsevich Filtered Backprojection (KFBP) helical reconstruction algorithm [12], [13]. The algorithm was originally developed for medical CT using a helical scan trajectory and has been shown that the KFBP algorithm can be employed advantageously in core imaging in typical micro-CT setups [13], [14]. KFBP provides theoretically exact reconstruction at any cone angle without cone-beam artifacts, which allows for significant improvement in scan throughput compared to step-and-shoot scanning.

## RESULTS

Contrast in acquired X-ray CT images depends on the energy of the X-ray. The mean X-ray energy from X-ray tube is 74.2 keV, 99.2 keV, and 123.0 keV for voltage setting of 110 kV, 160 kV, and 230 kV, respectively, calculated by using SpekCalc [16]. The X-ray energy spectrum is further modified by the sample under study. Fig. 1 shows the calculated X-ray energy spectra after traversing a 1 cm aluminum sample for three different voltages [17].

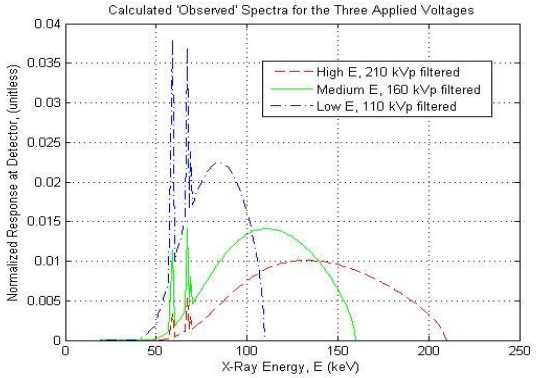


**Fig 1**. Normalized detector X-ray spectra for 110 keV, 160 keV, and 210 keV energy tube settings after passing through a 1 cm thick aluminum sample phantom calculated by SpekCalc.

Fig. 2 shows representative vertical slice from the X-ray (a) and neutron (b) tomography on the Middle East shale. In both images, the brighter areas indicate regions with larger attenuation, while the darker areas correspond to regions with less attenuation. For X-rays, the cross section of an element is proportional to its atomic number *Z* and the brighter areas indicate the regions containing more high-*Z* elements such as heavy minerals. For neutrons, the hydrogen-rich areas are brighter because hydrogen has a larger cross-section and attenuates neutron intensity more significantly. In Fig. 2, the regions outlined by the yellow ovals are bright in the X-ray image but dark in the neutron image and, therefore, are occupied by minerals including high-*Z* or high-density elements. In contrast, the regions outlined by the blue rectangles are dark on the X-ray image but bright in neutron image and are likely organic matter. The organic matter in this sample

forms continuous layered structures at the top, in the middle, and at the bottom of the sample. This is especially easy to see from the bright bands in the neutron image.

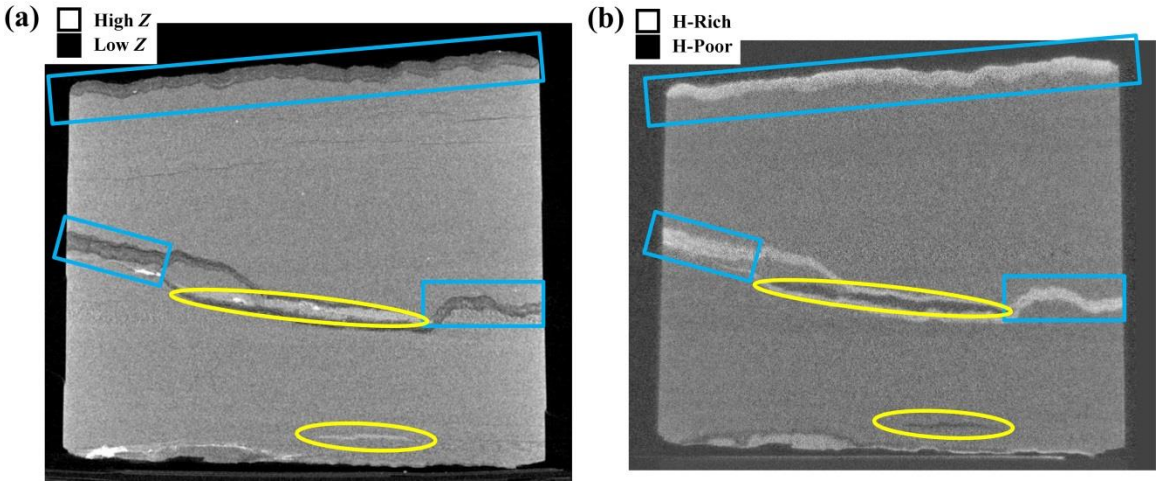


**Fig. 2** Representative vertical slice from X-ray (a) and neutron (b) tomography. Blue rectangles label regions of organic matter with lower attenuation in X-ray image but larger attenuation in neutron image. Yellow ovals label regions of high-*Z* minerals with higher attunation in X-ray but smaller atenuation in neutron image. Note that organic matter forms continuous layers in the sample.

Fig. 3 shows representative horizontal slice from X-ray (a) and neutron (b) tomography. As in Fig. 2, the blue rectangles mark regions including organic matter. It is worthwhile to point out that the black, linear feature in the X-ray image marked by the red rectangle can be easily mistaken for an open fracture if only the X-ray tomography is available. However, it is actually filled with organic matter, as revealed by neutron image; the same feature exhibits a larger attenuation coefficient than the matrix and is hydrogen rich. Also, as in Fig. 2, in Fig. 3 the yellow ovals mark regions with higher X-ray attenuation coefficients but smaller neutron attenuation coefficients. Considering the attenuation coefficient listed in Table 1, it is likely the yellow ovals highlight regions including pyrite while the green ovals mark region with anhydrite.

Fig. 4 shows horizontal slices from X-ray (a) and neutron (b) tomography which include a large area of continuous organic matter and a relatively homogenous matrix. These slices clearly demonstrate the opposite contrast between X-ray and neutron images and indicate that the neutron and X-ray images provide complementary information to each other on formation rocks.

Fig. 5 shows the 3D reconstructed images of the sample for X-ray (a) and neutron (b and c) modes, respectively. Fig. 5c displays only the high-attenuation regions and this gives the 3D distribution of organic matter in shale. Fig. 5c shows that

the organic matter forms clear layered structures in this sample with three layers: at the top, in the center, and at the bottom of the sample. In addition some organic matter is distributed throughout the sample.

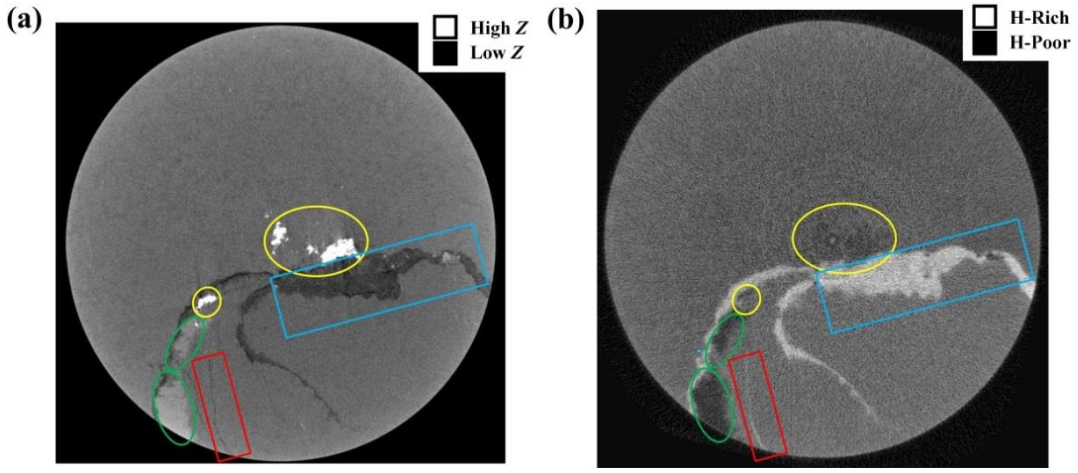


**Fig. 3** Representative horizontal slices from X-ray (a) and neutron (b) tomography. Rectangles mark regions of higher organic matter content with lower X-ray attenuation but larger neutron attenuation. The red rectangles mark an organic matter filled fracture. Yellow ovals label regions of high-*Z* minerals likely pyrite and green ovals contain likely anhydrite.

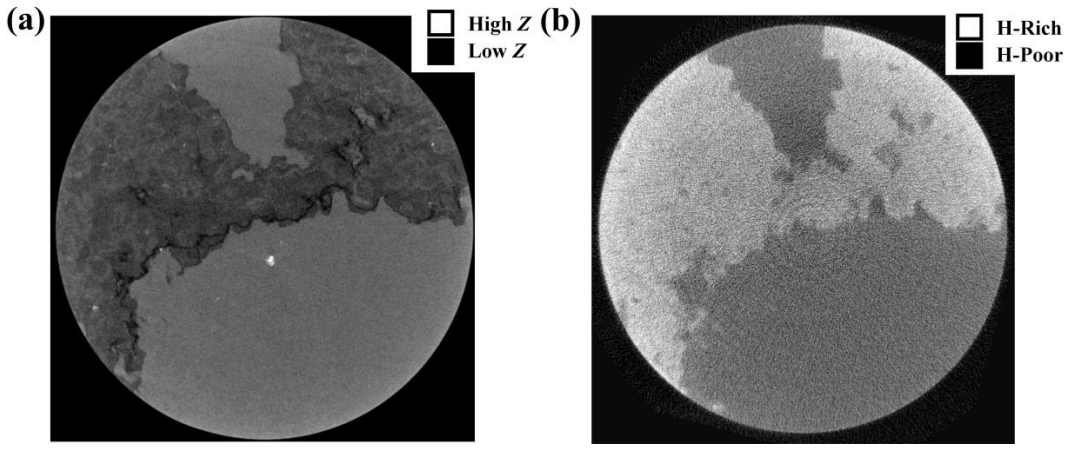


**Fig. 4** Horizontal slice from X-ray (a) and neutron (b) tomography showing opposite contrast between these two imaging technologies.

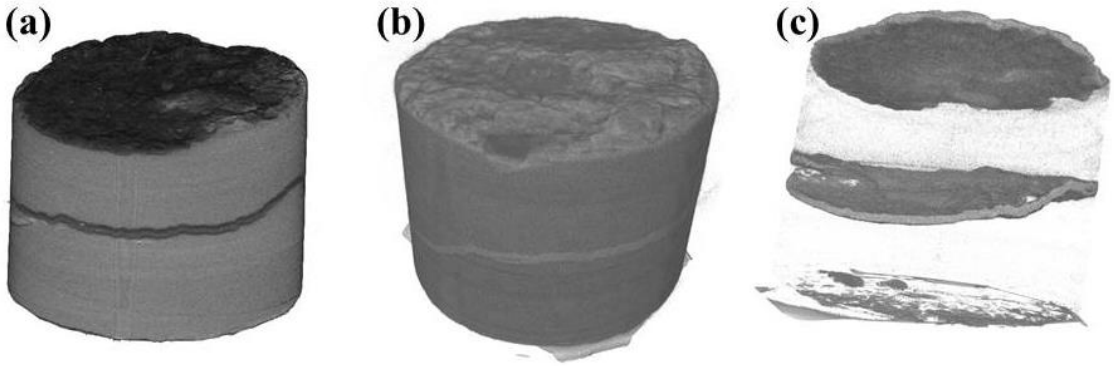


**Fig. 5** 3D volume renders of the shale sample for X-ray (a) and neutron (b) tomography and distribution of organic matter (c). Distribution of hydrogen-rich components, i.e. organic matter, is identified from the high-attenuated (bright) regions in 3D neutron tomography reconstructions.

## DISCUSSION

The distribution of different components within the shale rock is crucial for storage and transport of hydrocarbons in the shales. The Middle East shale in the current study is used as an example to demonstrate that dual X-ray and neutron tomography is a powerful tool to identify the distribution of minerals, kerogens, and fractures inside the shale rocks. Since the hydrogen-rich organic kerogens and fractures are both very transparent to X-rays, it is challenging for X-ray CT alone to unambiguously determine the kerogen distributions at the core scale. In contrast, neutrons are very sensitive to hydrogen and are useful to characterize the organic-rich shales. More comprehensive information of material composition and distributions in shale rocks can be obtained by combining X-ray and neutron image.

It is worth mentioning that the structures imaged in this study are on the core scale, rather than in pore scale. Current simulation and modeling of hydrocarbons are mostly based on the rock structure determined at the pore scale constructed from SEM images [18]–[21]. There is about a $10^9$ order of magnitude upscaling in length scale from pore scale to core scale. It is important to study the influence of the distribution of different components within the rocks by simulating and modeling the hydrocarbon flow at core scale and larger.

Since the wettability can be very different for the minerals and organic matter, the structure and arrangement in space of these components can directly affect the storage and transport of the hydrocarbons within the shale rocks. The laminar nature of organic-rich mud stones observed in the Middle East shale can dramatically change the current view of hydrocarbon flow and the mechanical properties in the shale rocks.

The organic-rich layers in Fig. 5 span the entire 25 mm diameter plug sample and seem to extend further to the full diameter core, although denser sampling is required to confirm this. The layered structure of the organic matter observed in this study has two important implications: first, the organic-rich bands have very different mechanical properties from the matrix and thus become the weak interfaces for the sample to break. The two ends of this sample were broken at the layer interfaces during plugging which is consistent with the assertion that the interface between organic-rich layer and inorganic-rich layer is a mechanical weak point. The organic layers in this sample are largely parallel to the formation bedding and, thus, perpendicular to the direction of hydraulic fracturing in a horizontal well. Their influence on hydraulic fracturing, however, remains unclear. From a nano-indentation study [22], organic matter was suggested to increase the tensile strength and raise the required pressure for hydraulic fracture initiation. However, the effects of these extensive organic-rich layers on hydraulic fracture require comprehensive study. Second, the organic matter layers can influence the flow of light hydrocarbons. If these layers are predominantly porous kerogen, they could form fast flow-paths for hydrocarbons. In contrast, if these layers are bitumen without pores, they would form barriers that would inhibit hydrocarbon flow. Further investigation is ongoing to delineate the properties of these organic matter layers. It can be argued that only the pore-networks among kerogens are important for light hydrocarbon flow in organic-rich shales. The neutron tomography may be the most sensitive approach to acquire the 3D distribution of kerogen in shale samples.

## CONCLUSIONS

Neutron imaging is more sensitive to hydrogen and X-ray imaging is more sensitive to high-Z minerals. The two methods are complementary and can reveal a more comprehensive structure of shales. The theoretical attenuation coefficients of typical components in shales for neutron and for X-ray tomography are presented in this study. The combination of neutron and X-ray tomography allows one to identify different minerals, fractures, and organic matter with voxel size of about 30 μm and field of view about 2 cm. The example shown in this study demonstrates the advantage of the combined use of these two imaging technologies: improved and more realistic representation of the rock 3D structure. The core scale 3D distribution of organic matter and fractures in these rocks could be used to simulate and model the hydrocarbon flow in the future. The layered structure of organic matter found in the studied shale sample is surprising and may significantly change the current explanations of hydrocarbon flow and rock mechanics in the studied reservoir.

## ACKNOWLEDGEMENTS

The authors would like to thank Aramco for allowing the publication of this work. We wish to thank Dr. Lorne Davis for calculating X-ray response shown in Fig. 1. The technical work has benefited from discussions with colleagues at Aramco Research Center-Houston: Younane Abousleiman and Hui-Hai Liu.

## REFERENCES

[1] Aloulou, F. and V. Zaretskaya, "Shale gas production drives world natural gas production growth - Today in Energy - U.S. Energy Information Administration (EIA)," 2016. [Online]. Available: https://www.eia.gov/todayinenergy/detail.php?id=27512. [Accessed: 11-Apr-2017].

[2] Chiang, W.-S., J. M. LaManna, D. S. Hussey, D. L. Jacobson, Y. Liu, D. T. Georgi, and J.-H. Chen, "Simultaneous Neutron and X-ray Imaging of 3D Kerogen and Fracture Structure in Shales," *SPWLA 58th Annual Logging Symposium*, (2017).

[3] Manke, I., C. Hartnig, M. Grünerbel, W. Lehnert, N. Kardjilov, A. Haibel, A. Hilger, J. Banhart, and H. Riesemeier, "Investigation of water evolution and transport in fuel cells with high resolution synchrotron X-ray radiography," *Appl. Phys. Lett.*, **90**, (2007), 174105.

[4] Banhart, J., A. Borbély, K. Dzieciol, F. Garcia-Moreno, I. Manke, N. Kardjilov, A. R. Kaysser-Pyzalla, M. Strobl, and W. Treimer, "X-ray and neutron imaging – Complementary techniques for materials science and engineering," *Int. J. Mater. Res.*, **101**, (2010),1069–1079.

[5] Manke, I., J. Banhart, A. Haibel, A. Rack, S. Zabler, N. Kardjilov, A. Hilger, A. Melzer, and H. Riesemeier, "*In situ* investigation of the discharge of alkaline Zn–MnO2 batteries with synchrotron X-ray and neutron tomographies," *Appl. Phys. Lett.*, **90**, (2007), 214102.

[6] Mannes, D., C. Benoît, D. Heinzelmann, and E. Lehmann, "Beyond the Visible: Combined Neutron and X-ray Imaging of an Altar Stone from the Former Augustinian Church in Fribourg, Switzerland," *Archaeometry*, **56**, (2014), 717–727.

[7] Mannes, D., F. Schmid, J. Frey, K. Schmidt-Ott, and E. Lehmann, "Combined Neutron and X-ray Imaging for Non-invasive Investigations of Cultural Heritage Objects," *Phys. Procedia*, **69**, (2015),653–660.

[8] "Neutron Activation Calculator." [Online]. Available: https://www.ncnr.nist.gov/resources/activation/. [Accessed: 27-Apr-2017].

[9] "NIST X-Ray Form Factor, Atten. Scatt. Tables Form Page." [Online]. Available: http://physics.nist.gov/PhysRefData/FFast/html/form.html. [Accessed: 27-Apr-2017].

[10] LaManna, J. M., D.S. Hussey, E. Baltic, and D. L. Jacobson, "Neutron and X-ray Tomography (NeXT) system for simultaneous, dual modality tomography,"

*Review of Scientific Instruments*, (2017).

[11] Limaye, A., "Drishti: a volume exploration and presentation tool," *Developments in X-Ray Tomography VIII*, (2012), 85060X.

[12] Katsevich, A., "Analysis of an exact inversion algorithm for spiral cone-beam CT," *Phys. Med. Biol.*, **47**, (2002), 302.

[13] Katsevich, A., M. Frenkel, M. Feser, Z. Huang, M. Andrew, T. Case, A. Gu, and W. Thompson, "New Fast and Accurate 3D Micro Computed Tomography Technology for Digital Core Analysis," *SPE Annual Technical Conference and Exhibition*, (2015).

[14] Sheppard, A., S. Latham, J. Middleton, A. Kingston, G. Myers, T. Varslot, A. Fogden, T. Sawkins, R. Cruikshank, M. Saadatfar, N. Francois, C. Arns, and T. Senden, "Techniques in helical scanning, dynamic imaging and image segmentation for improved quantitative analysis with X-ray micro-CT," *Nucl. Instruments Methods Phys. Res. Sect. B Beam Interact. with Mater. Atoms*, **324**, (2014), 49–56.

[15] Katsevich, A. and M. Frenkel, "TESTING OF THE CIRCLE AND LINE ALGORITHM IN THE SETTING OF MICRO-CT," *the International Symposium of the Society of Core Analysts*, (2016), SCA2016-080.

[16] Poludniowski, G. G. and P. M. Evans, "Calculation of X-ray spectra emerging from an X-ray tube. Part I. Electron penetration characteristics in X-ray targets," *Med. Phys.*, **34**, (2007), 2164–2174.

[17] Davis, L., "Development of a State-of-the-Art Petrophysical X-Ray CT for Unconventional Reservoirs," Personal Communication (2016).

[18] Saraji, S. and M. Piri, "The representative sample size in shale oil rocks and nano-scale characterization of transport properties," *Int. J. Coal Geol.*, **146**, (2015), 42–54.

[19] Chen, L., L. Zhang, Q. Kang, H. S. Viswanathan, J. Yao, and W. Tao, "Nanoscale simulation of shale transport properties using the lattice Boltzmann method: permeability and diffusivity," *Sci. Rep.*, **5**, (2015), 8089.

[20] Shabro, V., S. Kelly, C. Torres-Verdín, and K. Sepehrnoori, "Pore-Scale Modeling of Electrical Resistivity and Permeability in FIB-SEM Images of Hydrocarbon-Bearing Shale," *SPWLA 54th Annual Logging Symposium*, (2013).

[21] Jiang, W., M. Lin, Z. Yi, H. Li, and S. Wu, "Parameter Determination Using 3D FIB-SEM Images for Development of Effective Model of Shale Gas Flow in Nanoscale Pore Clusters," *Transp. Porous Media*, **117**, (2017), 5–25.

[22] Abousleiman, Y. N., K. L. Hull, Y. Han, G. Al-Muntasheri, P. Hosemann, S. Parker, and C. B. Howard, "The granular and polymer composite nature of kerogen-rich shale," *Acta Geotech.*, **11**, (2016), 573–594.

[23] Siskin, M., C. G. Scouten, K. D. Rose, T. Aczel, S. G. Colgrove, and R. E. Pabst, "Detailed Structural Characterization of the Organic Material in Rundle Ramsay Crossing and Green River Oil Shales," *Composition, Geochemistry and Conversion of Oil Shales*, Dordrecht: Springer Netherlands, (1995), 143–158.